

Multiple truly topological unidirectional surface magnetoplasmons at terahertz frequencies

Shengquan Fan,^{1,2,*} Tianjing Guo,^{2,*} Binbin Zhou,³ Jie Xu,⁴ Xiaohua Deng,² Jiangtao Lei,² Yun Shen,¹ Meicheng Fu,^{5,†} Kosmas L. Tsakmakidis,^{6,‡} and Lujun Hong^{2,§}

¹*School of Physical and Material, Nanchang University, Nanchang 330031, China*

²*Institute of Space Science and Technology, Nanchang University, Nanchang 330031, China*

³*Department of Electrical and Photonics Engineering,
Technical University of Denmark, Kongens Lyngby DK-2800, Denmark*

⁴*School of Medical Information and Engineering,
Southwest Medical University, Luzhou 646000, China*

⁵*College of Science, National University of Defense Technology, Changsha 410073, China*

⁶*Section of Condensed Matter Physics, Department of Physics,
National and Kapodistrian University of Athens Panepistimioupolis, Athens GR-157 84, Greece*

(Dated: January 17, 2025)

Unidirectional propagation based on surface magnetoplasmons (SMPs) has recently been realized at the interface of magnetized semiconductors. However, usually SMPs lose their unidirectionality due to non-local effects, especially in the lower trivial bandgap of such structures. More recently, a truly unidirectional SMP (USMP) has been demonstrated in the upper topological non-trivial bandgap, but it supports only a single USMP, limiting its functionality. In this work, we present a fundamental physical model for multiple, robust, truly topological USMP modes at terahertz (THz) frequencies, realized in a semiconductor-dielectric-semiconductor (SDS) slab waveguide under opposing external magnetic fields. We analytically derive the dispersion properties of the SMPs and perform numerical analysis in both local and non-local models. Our results show that the SDS waveguide supports two truly (even and odd) USMP modes in the upper topological non-trivial bandgap. Exploiting these two modes, we demonstrate unidirectional SMP multimode interference (USMMI), being highly robust and immune to backscattering, overcoming the back-reflection issue in conventional bidirectional waveguides. To demonstrate the usefulness of this approach, we numerically realize a frequency- and magnetically-tunable arbitrary-ratio splitter based on this robust USMMI, enabling multimode conversion. We, further, identify a unique index-near-zero (INZ) odd USMP mode in the SDS waveguide, distinct from conventional semiconductor-dielectric-metal waveguides. Leveraging this INZ mode, we achieve phase modulation with a phase shift from $-\pi$ to π . Our work expands the manipulation of topological waves and enriches the field of truly non-reciprocal topological physics for practical device applications.

I. INTRODUCTION

Topological electromagnetics (EM) [1–4] has gained significant attention due to its intriguing physics and potential applications [5]. One of the most remarkable features is the existence of unidirectional EM edge modes [6, 7] in non-trivial topological bandgaps, which can propagate in a single direction while suppressing backward reflection, even in the presence of defects [8, 9]. These unidirectional edge modes arise from the breaking of time-reversal symmetry through an external magnetic field [10, 11], and were first proposed as analogues of quantum Hall edge states [12, 13] in photonic crystals (PhCs) [14]. Such PhCs-based unidirectional modes have been demonstrated both theoretically [15, 16] and experimentally [17–22] at microwave frequencies.

As an alternative, surface magnetoplasmons (SMPs) have been proposed for unidirectional propagation due

to their simple and robust structure [23–28]. Recently, unidirectional SMPs (USMPs) have been realized using gyromagnetic (YIG) [29–32] and gyroelectric (InSb) [33–36] materials. In the terahertz (THz) regime, two types of USMP have been identified [37–39]. The first type, non-topological USMP, exists in the lower trivial bandgap of a magnetized semiconductor and transparent dielectric ($\epsilon_r > 0$) waveguide [36, 40, 41], maintaining unidirectional characteristics due to non-reciprocal flat asymptotes [36]. However, these SMPs lose their strict unidirectionality when non-local effects are included [42], as the asymptotes vanish [43]. The second type, truly topological USMPs, exist in the upper non-trivial bandgap [39, 44, 45], at the interface between magnetized semiconductors and opaque dielectrics ($\epsilon_r < 0$), and are immune to non-local effect. These genuinely topological USMPs were first theoretically proposed and shown to exhibit robust unidirectionality against non-locality [39], and later experimentally demonstrated in a magnetized InSb-metal waveguide [46]. Further, a low-loss broadband USMP in the upper bandgap was proposed in an InSb-Si-air-metal waveguide [47], though only one truly USMP mode is supported in these waveguides.

Moreover, multimode interference (MMI) has been

* These authors contributed equally to this work.

† fumeicheng10@nudt.edu.cn

‡ ktsakmakidis@phys.uoa.gr

§ ljhong@ncu.edu.cn

realized by coupling two or more conventional edge modes [48, 49], but these modes are bidirectional and suffer from back reflection. To overcome this limitation, PhCs-based MMI using multiple unidirectional modes has been proposed, effectively suppressing backscattering [50, 51]. More recently, unidirectional MMI based on PhCs has been experimentally demonstrated at microwave frequencies [52]. However, unidirectional MMI based on USMPs has not been reported at THz frequencies.

In this work, we propose a fundamental physical model for multiple truly USMP modes at THz frequencies, differing from previously proposed waveguides that support only one true USMP mode [39, 46, 47]. The model involves a semiconductor-dielectric-semiconductor (SDS) waveguide under opposing magnetic fields. We analytically derive and numerically analyze the dispersion in both local and non-local models, demonstrating that this waveguide supports two truly even and odd USMP modes in the upper bulk mode bandgap due to topological protection while these modes lose their unidirectionality in the lower bulk mode bandgap due to non-local effects. Using these two modes, we realize unidirectional SMP multimode interference (USMMI), which exhibits strong robustness against defects and eliminates backscattering, effectively overcoming the backscattering problem in conventional bidirectional waveguides; similarly to the PhCs-based MMI at microwave frequencies [52]. Additionally, we demonstrate a frequency- and magnetically-tunable arbitrary-ratio power splitter based on this robust USMMI, along with mode conversion capabilities. Notably, we report a unique index-near-zero (INZ) odd USMP mode in our waveguide, contrasting with conventional semiconductor-dielectric-metal waveguides that do not support the INZ mode [36]. This discovery enables efficient phase modulation with a phase shift of 2π .

II. THEORETICAL PHYSICAL MODEL

The basic physical model of multiple truly THz USMP modes in the SDS waveguide is illustrated in Fig. 1. In this part, we theoretically derive the dispersion equations for the SMP supported by the SDS structure in both local and non-local models.

A. Dispersion of SMP in the local model

First, we derive the dispersion equation of SMP in the local model. In our SDS system, the dielectric constant and thickness of the dielectric layer are ε_r and $2d$, respectively. To break the time-reversal symmetry of the system, opposing external magnetic fields (B_1 and B_2) are imposed on the semiconductors in the z direction. Consequently, the semiconductors exhibit gyroelectric anisotropy, with two corresponding relative permittivity tensors [36, 40]

tivity tensors [36, 40]

$$\varepsilon_{s1} = \begin{bmatrix} \varepsilon_{11} & i\varepsilon_{21} & 0 \\ -i\varepsilon_{21} & \varepsilon_{11} & 0 \\ 0 & 0 & \varepsilon_3 \end{bmatrix}, \varepsilon_{s2} = \begin{bmatrix} \varepsilon_{12} & -i\varepsilon_{22} & 0 \\ i\varepsilon_{22} & \varepsilon_{12} & 0 \\ 0 & 0 & \varepsilon_3 \end{bmatrix} \quad (1)$$

with $\varepsilon_{1j} = \varepsilon_\infty(1 - \frac{\bar{\omega}\omega_p^2}{\omega[\bar{\omega}^2 - \omega_{c_j}^2]})$, $\varepsilon_{2j} = \varepsilon_\infty \frac{\omega_{c_j}\omega_p^2}{\omega(\bar{\omega}^2 - \omega_{c_j}^2)}$ ($j = 1, 2$), and $\varepsilon_3 = \varepsilon_\infty(1 - \frac{\omega_p^2}{\bar{\omega}^2})$, where $\bar{\omega} = \omega + i\nu$, ν is the electron scattering frequency, $\omega_{c_j} = eB_j/m^*$ (where e and m^* are respectively the charge and effective mass of the electron) is the electron cyclotron frequency, ω_p is the plasma frequency, and ε_∞ is the high-frequency relative permittivity. In the magnetized semiconductor, the bulk modes have a dispersion relation of

$$k = \sqrt{\varepsilon_{vj}}k_0 \quad (2)$$

for transverse-magnetic (TM) polarization, where k is the propagation constant, $k_0 = \omega/c$ is the vacuum wavenumber, and $\varepsilon_{vj} = \varepsilon_{1j} - \varepsilon_{2j}/\varepsilon_{1j}^2$ is Voigt permittivity. It has two bandgaps with $\varepsilon_{vj} < 0$. The upper boundaries of the lower and upper bandgaps are $\omega_{aj} = \sqrt{\omega_{c_j}^2/4 + \omega_p^2} - \omega_{c_j}/2$ and $\omega_{bj} = \sqrt{\omega_{c_j}^2/4 + \omega_p^2} + \omega_{c_j}/2$ by $k = 0$ into Eq. (2). The lower boundary of the upper bandgaps are $\omega_{rj} = \sqrt{\omega_{c_j}^2 + \omega_p^2}$ by $k \rightarrow \pm\infty$ into Eq. (2). The waveguide supports TM polarized SMP. Solving Maxwell's equations with four continuous boundary conditions, the dispersion relation of SMP in the local model can be derived as (the details see Appendix A)

$$e^{4\alpha_d} = \prod_{j=1}^2 M_j \quad (3)$$

with

$$M_j = \frac{\varepsilon_{1j}\alpha_d\varepsilon_{vj} - \varepsilon_r(\varepsilon_{1j}\alpha_j - k\varepsilon_{2j})}{\varepsilon_{1j}\alpha_d\varepsilon_{vj} + \varepsilon_r(\varepsilon_{1j}\alpha_j - k\varepsilon_{2j})}$$

where $\alpha_d = \sqrt{k^2 - \varepsilon_r k_0^2}$, $\alpha_j = \sqrt{k^2 - \varepsilon_{vj} k_0^2}$. By substituting $k \rightarrow \pm\infty$ into Eq. (3), the forward (+) and backward (-) asymptotic frequencies are obtained as $\omega_{sp1}^\pm = \frac{1}{2}(\sqrt{\omega_{c_1}^2 + 4\omega_p^2 \frac{\varepsilon_\infty}{\varepsilon_\infty + \varepsilon_r}} \mp \omega_{c_1})$ and $\omega_{sp2}^\pm = \frac{1}{2}(\sqrt{\omega_{c_2}^2 + 4\omega_p^2 \frac{\varepsilon_\infty}{\varepsilon_\infty + \varepsilon_r}} \mp \omega_{c_2})$

Consider a special symmetric case of $B_1 = B_2$ (corresponding to $\omega_{c_1} = \omega_{c_2}$), we have $\varepsilon_{11} = \varepsilon_{12} = \varepsilon_1$, $\varepsilon_{21} = \varepsilon_{22} = \varepsilon_2$, $\varepsilon_{v1} = \varepsilon_{v2} = \varepsilon_v$ and $\alpha_1 = \alpha_2 = \alpha$, thus $M_1 = M_2$, then Eq. (3) becomes

$$\alpha - k \frac{\varepsilon_2}{\varepsilon_1} + \frac{\varepsilon_v}{\varepsilon_r} \alpha_d \tanh(\alpha_d d) = 0 \quad (4a)$$

$$\alpha - k \frac{\varepsilon_2}{\varepsilon_1} + \frac{\varepsilon_v}{\varepsilon_r} \alpha_d \coth(\alpha_d d) = 0 \quad (4b)$$

for the even and odd modes, respectively.

B. Dispersion of SMP in the non-local model

We further derive the dispersion equation of SMP in the non-local model. When non-local effects are introduced into our system as a hydrodynamic model of free-electron gas [53, 54], the response of the semiconductors to EM field gives rise to an induced free electron current \mathbf{J} [39, 42, 43], which satisfies the hydrodynamic equation $\beta^2 \nabla(\nabla \cdot \mathbf{J}) + \omega(\omega + i\nu)\mathbf{J} + i\omega\mathbf{J} \times \omega_c \hat{z} = i\omega\omega_p^2 \varepsilon_0 \varepsilon_\infty \mathbf{E}$, where β is the non-local parameter, and ν is a phenomenological damping rate. Maxwell's equations can be expressed as $\nabla \times \mathbf{H} = -i\omega\varepsilon_0\varepsilon_\infty \mathbf{E} + \mathbf{J}$ and $\nabla \times \mathbf{E} = i\omega\mu_0 \mathbf{H}$ due to non-local effect. The dispersion relation of bulk modes can be found as [39, 47]

$$Qk^4 + D_j k^2 + F_j = 0 \quad (5)$$

where $Q = \beta^2 \omega \bar{\omega}$, $D_j = (\beta^2 \varepsilon_\infty k_0^2 + \omega \bar{\omega})(\omega_p^2 - \omega \bar{\omega}) + \omega^2 \omega_{c_j}^2$, and $F_j = \varepsilon_\infty k_0^2 (\omega \bar{\omega} - \omega_p^2)^2 - \varepsilon_\infty k_0^2 \omega^2 \omega_{c_j}^2$. By solving Eq. (5), we obtain two dispersion relations for the upper and lower bulk modes: $k_{aj}^2 = (-D_j + \sqrt{D_j^2 - 4QF_j})/2Q$ and $k_{bj}^2 = (-D_j - \sqrt{D_j^2 - 4QF_j})/2Q$, where the lower cut-off frequencies are identical to ω_{aj} and ω_{bj} in the local model. Here, k_{aj} and k_{bj} are the propagation constants. In contrast to the local model, the upper cutoff frequency ω_{r_j} does not exist in the non-local model.

Combining hydrodynamic and Maxwell's equations with six continuous boundary conditions, the SMP dispersion in the non-local model can be expressed as (the details see Appendix B)

$$e^{4\alpha_d d} = \prod_{j=1}^2 N_j \quad (6)$$

with

$$N_j = \frac{\varepsilon_\infty \alpha_d / \varepsilon_r (\gamma_j s_j + i p_j s'_j) + k(\gamma_j + i p_j) + (k^2 - k_0^2 \varepsilon_\infty)(s'_j - s_j)}{\varepsilon_\infty \alpha_d / \varepsilon_r (\gamma_j s_j + i p_j s'_j) - k(\gamma_j + i p_j) - (k^2 - k_0^2 \varepsilon_\infty)(s'_j - s_j)}$$

where $\gamma_j = \sqrt{k^2 - k_{bj}^2}$, $p_j = \sqrt{k_{aj}^2 - k^2}$, and

$$s_j = \frac{\omega \bar{\omega} p_j^2 + i\omega \omega_{c_j} k p_j + \varepsilon_\infty k_0^2 [\beta^2 k^2 - \omega \bar{\omega} + \omega_p^2]}{\omega \omega_{c_j} (k^2 - \varepsilon_\infty k_0^2) - i(\omega \bar{\omega} - \varepsilon_\infty \beta^2 k_0^2) k p_j}$$

$$s'_j = \frac{-\omega \bar{\omega} \gamma_j^2 - \omega \omega_{c_j} k \gamma_j + \varepsilon_\infty k_0^2 [\beta^2 k^2 - \omega \bar{\omega} + \omega_p^2]}{\omega \omega_{c_j} (k^2 - \varepsilon_\infty k_0^2) + (\omega \bar{\omega} - \varepsilon_\infty \beta^2 k_0^2) k \gamma_j}$$

Consider a special symmetric case, we have $s_1 = s_2 = s$, $s'_1 = s'_2 = s'$, $p_1 = p_2 = p$ and $\gamma_1 = \gamma_2 = \gamma$; thus $N_1 = N_2$; Eq. (6) becomes

$$\varepsilon_\infty \alpha_d / \varepsilon_r (\gamma s + i p s') \tanh(\alpha_d d) + (s - s')(k^2 - k_0^2 \varepsilon_\infty) - k(\gamma + i p) = 0 \quad (7a)$$

$$\varepsilon_\infty \alpha_d / \varepsilon_r (\gamma s + i p s') \coth(\alpha_d d) + (s - s')(k^2 - k_0^2 \varepsilon_\infty) - k(\gamma + i p) = 0 \quad (7b)$$

for the even and odd modes, respectively.

III. SIMULATION RESULTS

In this part, we conduct a detailed numerical analysis of the SMP dispersion based on the derived equations in the SDS system and demonstrate many degrees of freedom to manipulate SMP modes, including interference, power, and phase, by full-wave simulation. Throughout the paper, the semiconductor is assumed to be InSb with $\varepsilon_\infty = 15.7$, $\omega_p = 4\pi \times 10^{12}$ rad/s ($f_p = 2$ THz), and the dielectric layer is exemplified by silicon with a relative permittivity of $\varepsilon_r = 11.68$.

A. The dispersion in the lower bulk mode bandgap

We first analyze the dispersion of SMP within the lower bulk mode bandgap. This bandgap ranges from 0 to ω_{a_2} , where $\omega_{a_2} = \sqrt{\omega_{c_2}^2/4 + \omega_p^2} - \omega_{c_2}/2$ when $\omega_{c_2} \geq \omega_{c_1}$. The special case of the symmetric ($\omega_{c_2} = \omega_{c_1}$) waveguide is considered. Using Eqs. (4) and (7), we numerically calculate the dispersion relations of SMPs in both local and non-local models, respectively. In the calculation, we ignore the effect of material loss (i.e., $\nu = 0$) and take $d = 0.04\lambda_p$ as an example. Figure 1(a) shows the dispersion of SMP in the symmetric waveguides for $\omega_{c_1} = \omega_{c_2} = 0.25\omega_p$, corresponding to $B_1 = B_2 = 0.25$ T. As

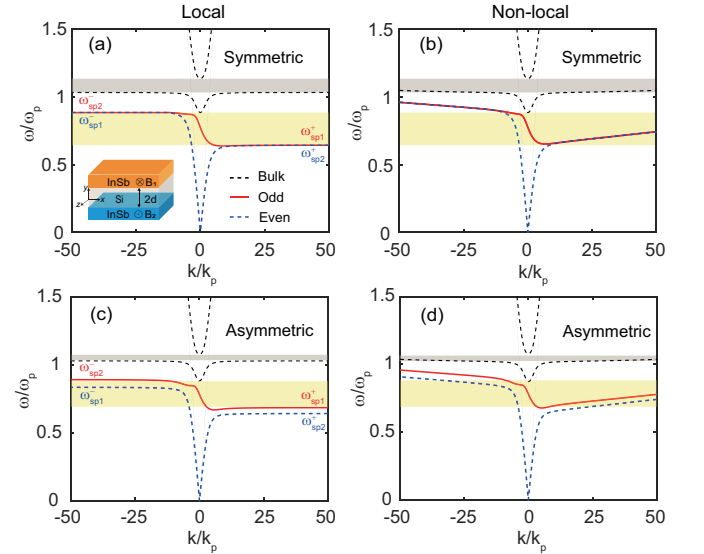


FIG. 1. Dispersion relation of SMP in the lower bulk mode bandgap for the local (a, c) and non-local (b, d) model. (a, b) show the symmetric waveguide for $\omega_{c_1} = \omega_{c_2} = 0.25\omega_p$, while (c, d) show the asymmetric waveguide for $\omega_{c_1} = 0.15\omega_p$ and $\omega_{c_2} = 0.25\omega_p$. The solid red and dashed blue lines show the odd and even SMP modes. The inset shows the schematic of the SDS waveguide. $\omega_{c_1} = 0.15\omega_p$ and $\omega_{c_2} = 0.25\omega_p$, correspond to the external magnetic fields $B_1 = 0.15$ T and $B_2 = 0.25$ T, respectively. The non-local parameter is $\beta = 1.07 \times 10^6$ m/s, and the other parameters are $\varepsilon_\infty = 15.7$, $\varepsilon_r = 11.68$, $d = 0.04\lambda_p$, and $\omega_p = 4\pi \times 10^{12}$ rad/s.

expected, the SDS structure supports two SMP modes: odd mode (solid red line) and even mode (dashed blue line). These two modes exhibit identical asymptotic frequencies ($\omega_{sp1}^- = \omega_{sp2}^-$, $\omega_{sp1}^+ = \omega_{sp2}^+$). Moreover, these two modes propagate backward only within the frequency range $[\omega_{sp}^-, \omega_{a2}]$, corresponding to $[0.6425\omega_p, 0.8828\omega_p]$; As a result, a unidirectional propagation range is formed, as seen in the shaded yellow region in Fig. 1(a). However, when the non-local effects (non-local parameter $\beta = 1.07 \times 10^6$ m/s) are taken into account, the dispersion curves of the SMP modes differ significantly, as shown in Fig. 1(b). The forward and backward asymptotic frequencies of both modes vanish at large wave numbers, leading to the disappearance of the unidirectional propagation region within the lower bulk mode bandgap.

To further investigate the phenomenon of unidirectional disappearance induced by non-local effects, we analyze the dispersion in the common case of asymmetric waveguide ($\omega_{c2} \neq \omega_{c1}$) using Eqs. (3) and (6). As an example, $\omega_{c1} = 0.15\omega_p$ and $\omega_{c2} = 0.25\omega_p$, which correspond to $B_1 = 0.15$ T and $B_2 = 0.25$ T, and the other parameters are identical to those of the symmetric waveguide. Figure 1(c) shows the dispersion curve for the local model. Due to the asymmetric structure, the SMP waveguide also supports even and odd modes. The asymptotic frequencies for the odd modes are ω_{sp2}^- and ω_{sp1}^+ , while those for the even modes are ω_{sp1}^- and ω_{sp2}^+ . As seen in the yellow shaded region, a unidirectional window based on horizontal asymptotes clearly occurs in $[\omega_{sp1}^+, \omega_{a2}]$, corresponds to $[0.6859\omega_p, 0.8828\omega_p]$. For comparison, the dispersion curve for the non-local model is numerically calculated using Eq. (6). Similarly to the symmetric waveguide, Fig. 1(d) further demonstrates the disappearance of the asymptotic frequency when considering non-local effects, leading to the absence of the USMP window in the asymmetric waveguide. Therefore, the results demonstrate that for both symmetric and asymmetric waveguides, the SMP modes lose their unidirectionality in the lower bulk mode bandgap when non-local effects are considered.

B. The dispersion in the upper bulk mode bandgap

We further analyze the dispersion of SMP in the upper bulk mode bandgap $[\omega_{r2}, \omega_{b1}]$, where $\omega_{r2} = \sqrt{\omega_{c2}^2 + \omega_p^2}$ and $\omega_{b1} = \sqrt{\omega_{c1}^2/4 + \omega_p^2} + \omega_{c1}/2$, corresponding to the gray region in Fig. 1. We numerically calculate the dispersion of SMP in the local model, and the parameters are consistent with those in Fig. 1. Figure 2(a) shows the dispersion diagram for the symmetric waveguide with $\omega_{c1} = \omega_{c2} = 0.25\omega_p$. As seen from the lines, this symmetric waveguide supports both odd (red solid line) and even (blue dashed line) USMP modes in upper bulk mode bandgap $[\omega_{r2}, \omega_{b2}]$, which corresponds to $[1.0308\omega_p, 1.1328\omega_p]$, marked by the grey shaded area.

For comparison, the dispersion of SMP in the non-local model is also shown as circles in Fig. 2(a). Obviously, the dispersion curves for odd and even SMP modes almost completely coincide for both the local and non-local models. In contrast to the lower trivial bandgap, the SMP modes maintain their unidirectionality for small wavenumbers in the upper topologically non-trivial bandgap, even when non-local effects are considered. Figure 2(b) illustrates the dispersion curves for the asymmetric waveguide with $\omega_{c1} = 0.15\omega_p$ and $\omega_{c2} = 0.25\omega_p$. Similarly to the symmetric results in Fig. 2(a), the USMP modes still exist, and the lines and circles almost completely overlap. However, the USMP band is compressed to the range $[1.0308\omega_p, 1.0778\omega_p]$, resulting from the asymmetric structure. When $\omega_{c2} \geq \omega_{c1}$, the USMP bandwidth $\Delta\omega = \omega_{b1} - \omega_{r2}$ is characterized by

$$\Delta\omega = \sqrt{\omega_{c1}^2/4 + \omega_p^2} + \omega_{c1}/2 - \sqrt{\omega_{c2}^2 + \omega_p^2} \quad (8)$$

Note that when $\omega_{c2} < \omega_{c1}$, the roles of ω_{c1} and ω_{c2} in the Eq. (8) will be interchanged. Figure 2(c) illustrates the variation of bandwidth $\Delta\omega$ with respect to ω_{c1} and ω_{c2} , which correspond to related parameters B_1 and B_2 . Due to $\omega_{c1} = eB_1/m^*$ and $\omega_{c2} = eB_2/m^*$, the unidirectional bandwidth $\Delta\omega$ is magnetically-controllable by varying B_1 and B_2 . It is found that $\Delta\omega$ exhibits a local maximum when $\omega_{c1} = \omega_{c2}$. The white dashed line indicates the distribution of this local maximum, which increases with ω_{c2} .

These results confirm that in the upper bandgap, our waveguide supports two truly USMP modes at THz frequencies. The even and odd USMP modes maintain their unidirectionality when considering non-local effects, which is different from the situation in the lower bandgap. Moreover, the unidirectional characteristics of the SMP modes are equivalent in both the local and non-local models. Therefore, we will take the local model in the subsequent numerical calculations and simulations as an example, and our interest focuses on the upper bulk mode bandgap.

C. Unidirectional MMI based on two USMP modes

When two USMP modes are excited simultaneously and interact with each other in the silicon layer, unidirectional SMP multimode interference (USMMI) emerges. To verify this phenomenon, we simulate wave transmission in both symmetric and asymmetric waveguides with the finite element method (FEM) using COMSOL Multiphysics, as shown in Fig. 2(d). In the simulation, we position a magnetic current point source with a frequency of $\omega = 1.05\omega_p$ to excite the SMP and take into account the material loss (i.e., $\nu = 10^{-6}\omega_p$). As expected, USMMI is realized at THz frequencies, and it can only propagate forward, not backward, in both symmetric and asym-

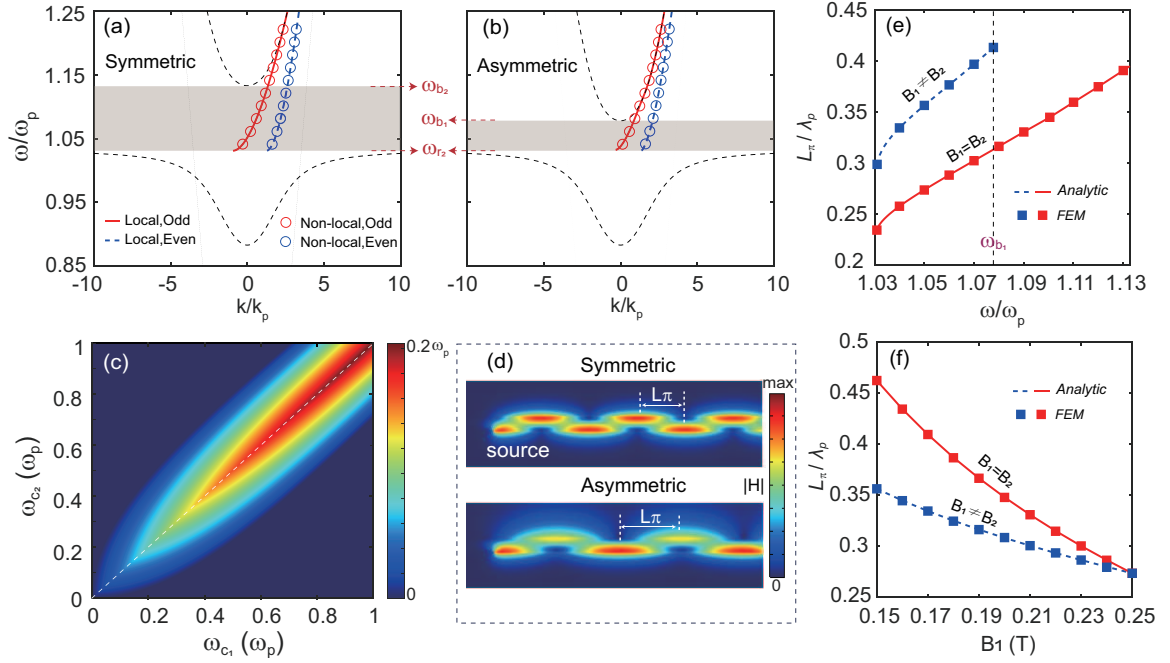


FIG. 2. (a, b) Dispersion relations of SMPs in the upper bulk mode bandgap. (a) The symmetric waveguide for $\omega_{c1} = \omega_{c2} = 0.25\omega_p$, and (b) the asymmetric waveguide for $\omega_{c1} = 0.15\omega_p$ and $\omega_{c2} = 0.25\omega_p$, corresponds to $B_1 = 0.15$ T and $B_2 = 0.25$ T. The dispersion curves almost perfectly coincide for the local (lines) and non-local (circles) models. The blue and red show the even and odd SMP modes, respectively. The shaded yellow areas represent the USMP band. (c) The USMP bandwidth $\Delta\omega$ as a function of ω_{c1} and ω_{c2} , and the dashed white line corresponds to $\omega_{c1} = \omega_{c2}$. (d) H -field distributions in the symmetric and asymmetric waveguide at $\omega = 1.05\omega_p$. (e, f) The analytical (line) and FEM (square) results of beat length L_π as a function of frequency ω and external magnetic field B_1 , respectively. The blue and red represent $B_1 \neq B_2$ and $B_1 = B_2$, respectively. The dashed black line corresponds to $\omega_{b1} = 1.0778\omega_p$. The other parameters are the same as in Fig. 1.

metric waveguides. The H -field distribution in the symmetric waveguide is identical at both InSb-Si interfaces, whereas it differs in the asymmetric waveguide due to structural asymmetry. Moreover, the H -fields of USMMI are periodic with a period of $2L_\pi$, where the beat length L_π is denoted by [50, 55]

$$L_\pi = \frac{\pi}{k_{\text{even}} - k_{\text{odd}}} \quad (9)$$

where k_{even} (k_{odd}) is the propagation constant of the even (odd) mode, respectively.

To further investigate the characteristics of USMMI, we analyze the variation of L_π with frequency and the external magnetic field. Figure 2(e) shows the analytical value of L_π as a function of ω using Eq. (9) in the whole USMMI range. It is evident that L_π increases with ω for both symmetric ($B_1 = B_2 = 0.25$ T) and asymmetric ($B_1 = 0.15$ T and $B_2 = 0.25$ T) waveguides, corresponding to the red and blue lines, respectively. Figure 2(f) shows L_π as a function of B_1 , where ω is fixed at $1.05\omega_p$ as an example. As seen from the solid red line, the analytical L_π monotonically decreases with B_1 varying from 0.15 T to 0.25 T, demonstrating the magnetically-controllable properties of USMMI by tuning two symmetric magnetic fields ($B_1 = B_2$). More interestingly, we achieve magnetically-controllable L_π with a single-sided

magnetic field, as indicated by the dashed blue line in Fig. 2(f). Here, B_2 is fixed at 0.25 T as an example. L_π monotonically decreases with B_1 . Furthermore, we select multiple frequencies and magnetic fields to calculate the simulated L_π with the full-wave FEM, as seen in the squares in Figs. 2(e) and 2(f), respectively. Obviously, the FEM results are in perfect agreement with the analytical values. Note that USMMI persists in the whole range, resulting from the magnetically-controllable USMMI band. This result confirms that USMMI is controllable by both frequency and the external magnetic field.

D. Frequency- and magnetically-tunable arbitrary-ratio power splitter based on USMMI

By controlling the beat length L_π of MMI with external magnetic fields and frequencies, power manipulation has been achieved in topological PhCs at microwave frequencies [52]. Here, utilizing USMMI, we achieve arbitrary ratio power manipulation at THz frequencies. To verify this, we propose an H-shaped splitter, as shown in Fig. 3(a). The middle part is an SDS waveguide supporting USMMI, while the left and right parts are InSb-Si-Metal waveguides with silicon thickness d [36], which

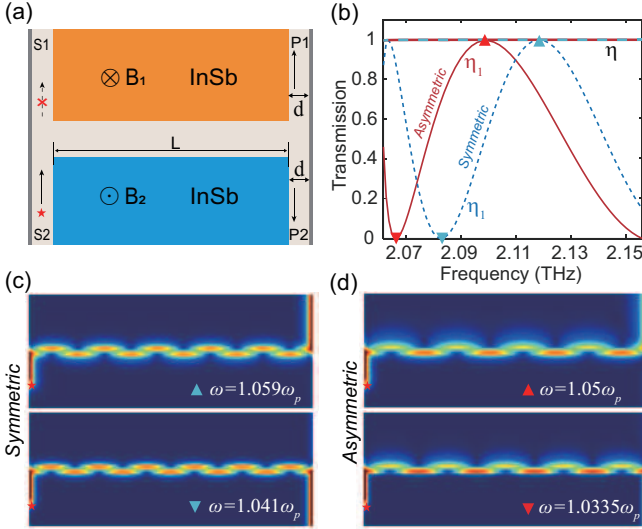


FIG. 3. Arbitrary ratio power manipulation by frequency. (a) Schematic of the H-shaped splitter based on USMMI. (b) Transmission of SMP along channel P1 (η_1) and total transmission (η) in the symmetric and asymmetric splitters. (c,d) Simulated H-field amplitudes in the symmetric splitter at $\omega = 1.059\omega_p$ and $\omega = 1.041\omega_p$ (c), and the asymmetric splitter at $\omega = 1.05\omega_p$ and $\omega = 1.0335\omega_p$ (d). The parameters are the same as in Fig. 2.

has the same dispersion equation as given in Eq. (4a). A source, marked by a star, is placed at the input channel S2 to excite USMP and USMMI. Consequently, it is divided into the upper and lower outputs labeled as P1 and P2, respectively. To illustrate this, we perform full-wave simulations in both symmetric ($B_1 = B_2 = 0.25$ T) and asymmetric ($B_1 = 0.15$ T, $B_2 = 0.25$ T) waveguides, and define the power ratio of channel P1 (P2) to channel S2 as $\eta_1(\eta_2)$, and the total transmission as $\eta = \eta_1 + \eta_2$.

Figure 3(b) displays the transmission coefficients η_1 and η versus ω for both splitters. η_1 oscillates arbitrarily between 0 and 1 in the unidirectional range from $1.0308\omega_p$ to $1.0778\omega_p$. Owing to the backscattering-immune property of topologically USMP mode and the absence of reflection at the corners, η remains close to 1 under low-loss conditions. For the symmetric waveguide, $\eta_1 = 0$ ($\eta_2 = 1$) at $\omega = 1.041\omega_p$ and $\eta_1 = 1$ ($\eta_2 = 0$) at $\omega = 1.059\omega_p$; whereas for the asymmetric waveguide, $\eta_1 = 0$ ($\eta_2 = 1$) at $\omega = 1.0335\omega_p$ and $\eta_1 = 1$ ($\eta_2 = 0$) at $\omega = 1.05\omega_p$. For clarity, the H distributions of both waveguides are presented in Figs. 3(c) and 3(d), respectively. As expected, the power almost entirely flows into Channels P1 and P2 at $\omega = 1.059\omega_p$ and $1.041\omega_p$, and the interference length L satisfies $L \approx 10.5L_{\pi(\omega=1.059\omega_p)} \approx 11.5L_{\pi(\omega=1.041\omega_p)}$ with an inverted (direct) image at the corner in the symmetric waveguide. Similarly, the power flow into Channel P1 (P2) at $\omega = 1.05\omega_p$ ($1.0335\omega_p$), with $L \approx 8.5L_{\pi(\omega=1.05\omega_p)} \approx 9.5L_{\pi(\omega=1.0335\omega_p)}$ in the asymmetric waveguide. The results demonstrate that a frequency-tunable arbitrary-ratio power splitter is realized using

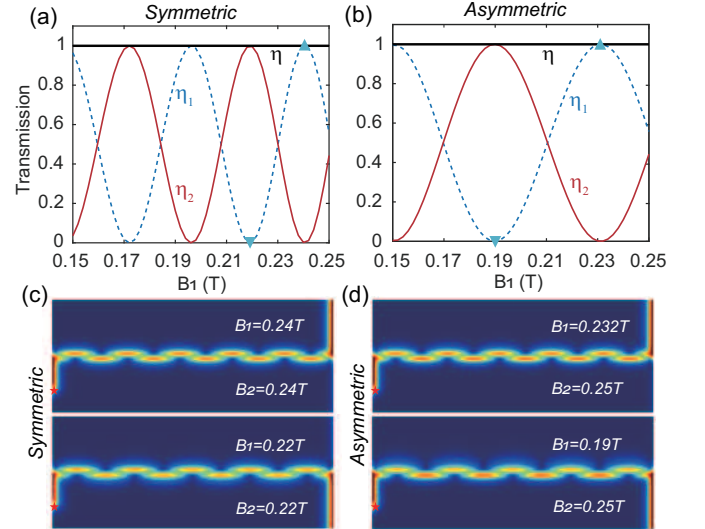


FIG. 4. Arbitrary ratio power manipulation by the external magnetic field. (a,b) Transmission coefficients η_1 , η_2 , and η as functions of magnetic fields B_1 . (a) $B_1 = B_2$, (b) $B_1 \neq B_2$, and B_2 is fixed at 0.25 T. (c,d) Simulated H-field amplitudes in the symmetric (a) splitter at $B_1 = B_2 = 0.24$ T and $B_1 = B_2 = 0.22$ T (c), and the asymmetric (b) splitter at $B_1 = 0.232$ T and $B_1 = 0.19$ T (d). The working frequency is fixed at $\omega = 1.05\omega_p$.

USMMI.

Furthermore, the magnetically-tunable power splitter based on USMMI is demonstrated. To verify this, the frequency is fixed at $\omega = 1.05\omega_p$. Figure 4(a) shows the η_1 , η_2 , and η versus B_1 by tuning two symmetric magnetic fields ($B_1 = B_2$). η_1 and η_2 vary continuously from 0 to 1 as B_1 changes within the range of [0.15 T, 0.25 T]. As a special case, $\eta_1 = 0$ and $\eta_2 = 1$ at $B_1 = B_2 = 0.22$ T, and $\eta_1 = 1$ and $\eta_2 = 0$ at $B_1 = B_2 = 0.24$ T. The corresponding full-wave simulation results are displayed in Fig. 4(c). As expected, the power respectively flows into channel P1 (P2) at $B_1 = 0.22$ T (0.24 T), and the values of L satisfy $L \approx 10.5L_{\pi(B_1=0.24T)} \approx 9.5L_{\pi(B_1=0.22T)}$ with an inverted (direct) image at the corner. This result confirms the arbitrary ratio power manipulation by the magnetic field. More importantly, we propose a single-sided magnetic control power splitter, which is much easier to operate than the both-sided control in practical applications. To demonstrate this, we set a fixed value of $B_2 = 0.25$ T as an example and resimulate by only adjusting B_1 . As seen in Fig. 4(b), the splitter achieves arbitrarily splitting ratios from 0 to 1 as expected. When $B_1 = 0.232$ T and $B_1 = 0.19$ T, the power is respectively directed to channels P1 and P2, as shown in Fig. 4(d), demonstrating magnetically-controllable power manipulation with only one magnetic field. Therefore, a USMMI-based power splitter has been demonstrated to achieve arbitrary ratios of power manipulation by the external magnetic field intensity and frequency, resulting from the frequency- and magnetically-controllable USMMI.

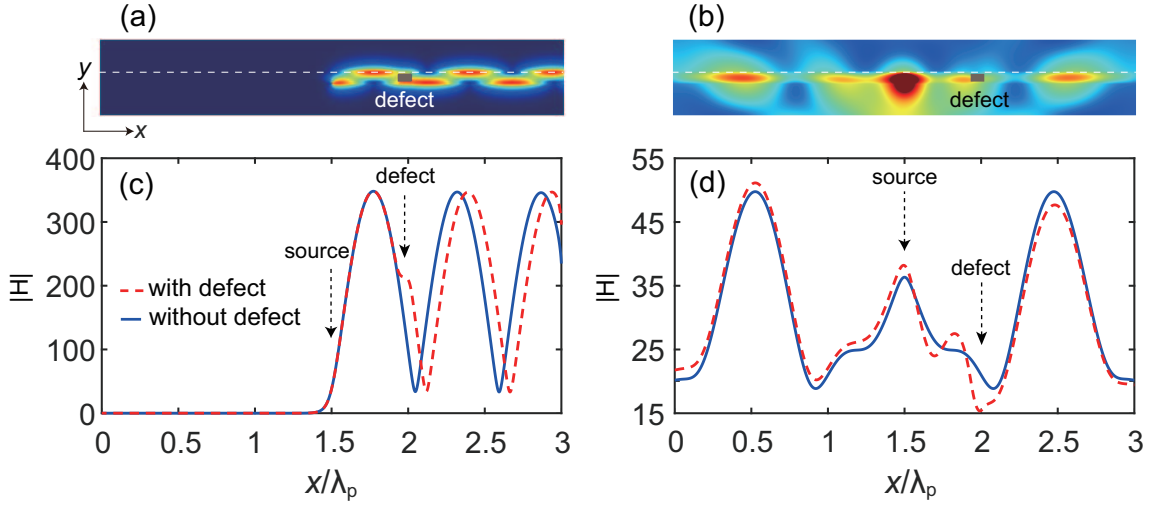


FIG. 5. Comparison of our unidirectional waveguide with conventional waveguide. (a,b) Simulated H -field amplitudes of the symmetric waveguide. (a) Robust USMP modes without backscattering. (b) A conventional bidirectional mode with backscattering from the metallic defect. (c, d) H -field distributions with (solid lines) and without (dashed lines) the defects along the upper InSb-Si interface. The operating frequency is $\omega = 1.05\omega_p$ and other parameters are the same as in Fig. 3

E. Robust USMMI at THz frequencies

To demonstrate the robustness of the USMMI, we introduce a square metallic defect of $0.04\lambda_p \times 0.08\lambda_p$ into the waveguide, as highlighted by the grey part in Fig. 5(a). We take a symmetric waveguide as an example. Figure 5(a) shows the simulated H -field amplitudes for $\omega = 1.05\omega_p$. It can be seen that the excited USMMI mode can smoothly bypass the defect and still travel forward without generating a backward wave from the defect. To clearly illustrate this phenomenon, the H -field distributions along the upper InSb-Si interface are displayed for both cases with (dashed line) and without (solid line) defects in Fig. 5(c). As expected, the fields of USMMI remain unchanged before the defect and quickly recover the same amplitude after it. These results confirm the strong robustness of USMMI.

For comparison, we remove the external magnetic field from the waveguide in Fig. 5(a), effectively making it a conventional waveguide and resimulating it. Fig. 5(b) shows the simulated H -field amplitudes with the defect. The excited wave is transmitted bidirectionally, and the H -field radiates everywhere in this waveguide. To clearly show this, the H -field distributions for conventional waveguides with and without defects are plotted in Fig. 5(d). Without defects, the forward and backward fields are symmetric (solid line). When the defect is introduced, the field amplitudes become asymmetric (dashed line), with an increase before the defect and a decrease after it, demonstrating the backward reflection induced by the defect. These results demonstrate that our waveguide supports a robust USMMI mode without backscattering against defects, in contrast to the conventional bidirectional waveguide with backscattering.

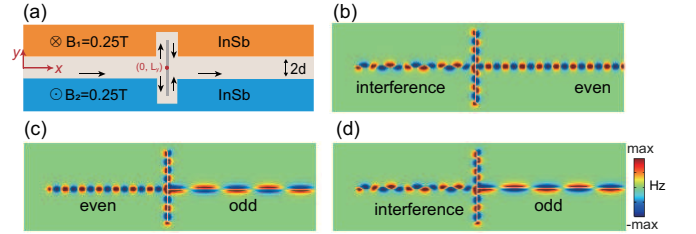


FIG. 6. (a) Schematic of multiple SMP modes conversion based on the symmetric splitter. Simulated H_z field amplitudes for $\omega = 1.08\omega_p$. The interference modes are converted to odd (b) and even (d) modes. (c) The even mode is converted to the odd mode.

F. Multiple modes conversion and phase modulation based on USMP

Based on the splitter, we further design a structure to achieve the conversion among multiple modes, as shown in Fig. 6(a). In this structure, the left and right parts are symmetric waveguides, and the silicon thickness is d in the middle part. The input mode is equally divided and then recombines into a single output mode, with a phase difference $\Delta\varphi = \varphi_0 + 4kL_y$, where φ_0 is the initial phase difference, and L_y is the position of the center of the metal bar along the y -axis. It is found that the incident mode can be converted to an even mode when $\Delta\varphi = 2n\pi$ (where n is an integer) and to an odd mode when $\Delta\varphi = (2n+1)\pi$. The mode conversion satisfies the equations

$$L_y = \begin{cases} \frac{2n\pi - \varphi_0}{4k} & \text{for even mode,} \\ \frac{(2n+1)\pi - \varphi_0}{4k} & \text{for odd mode.} \end{cases} \quad (10)$$

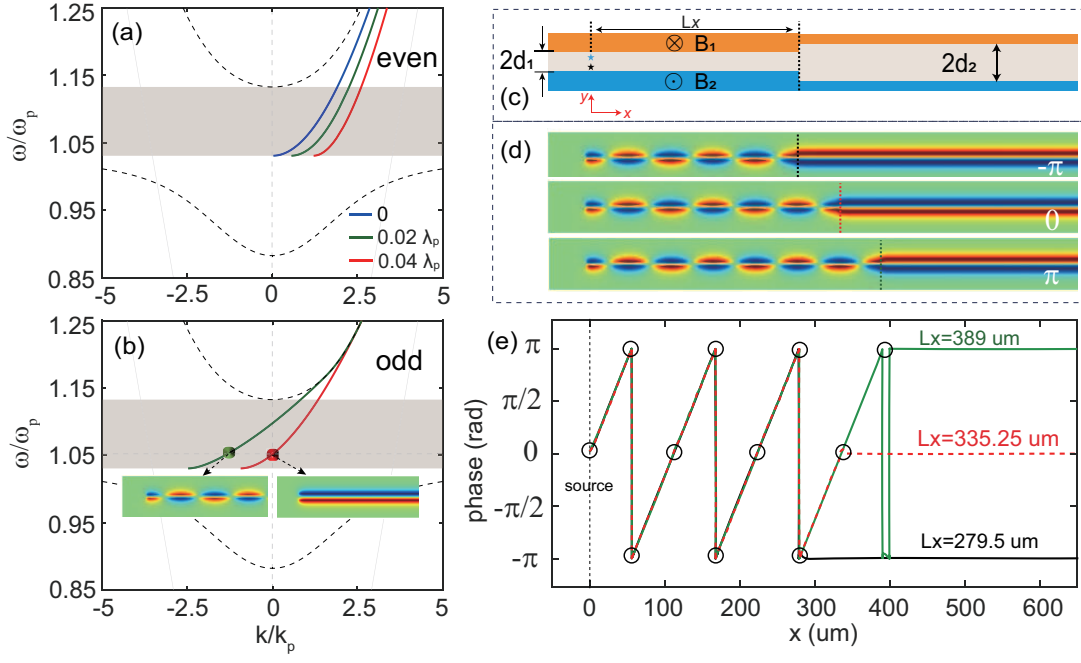


FIG. 7. (a,b) The dispersion of even and odd modes for different d values in the symmetric SDS waveguide. Insets in (b) show H_z field amplitudes of normal (green dot) and INZ (red dot) mode at $\omega = 1.0517\omega_p$. (c) The schematic of phase modulator by connecting two SDS waveguides with d . (d) Simulated H_z field amplitudes at $\omega = 1.0517\omega_p$. (e) The phase of H_z is the output INZ modes along the lower InSb-Si interface for the phase modulation (d). The parameters are $d_1 = 0.02\lambda_p$ and $d_2 = 0.04\lambda_p$.

where $n = \dots -2, -1, 0, 1, 2, \dots$, this indicates that multi-mode conversion can be realized by tuning L_y . We first consider a special case of mode conversion from an even mode to an odd mode, where $\varphi_0 = 0$. Here, we take $\omega = 1.08\omega_p$ as an example, corresponding to $k = 2.153k_p$. Thus, the theoretical value is found to be $L_y = 0.0580\lambda_p$ for $n = 0$ using Eq. (10). To verify this, we perform full-wave simulations and the simulated H_z -field for $\omega = 1.08\omega_p$ is displayed in Fig. 6(c). The even mode is converted into odd modes when $L_y = 0.0580\lambda_p$ as expected. Furthermore, our FEM simulations demonstrate that the USMMI mode is converted into both even and odd modes when $L_y = -0.0283\lambda_p$ and $L_y = 0.0297\lambda_p$, as shown in Figs. 6(b) and 6(d). It is found that $\varphi_0 = 0.4882\pi$, and the values of L_y also satisfy Eq. (10) when $n = 0$. The results demonstrate that our structure achieves not only the conversion between USMMI and single mode but also the conversion between odd and even modes.

Interestingly, we further discover a unique index-near-zero (INZ) odd USMP mode without phase variation ($k = 0$) supported by the SDS waveguide at THz frequencies, which is distinct from USMP in the conventional InSb-Si-Metal waveguides [32, 36]. These waveguides do not support INZ mode in the upper non-trivial bandgap. Based on the INZ odd mode in our waveguide, THz phase modulation is achieved. To illustrate this, we first calculate the dispersion curves of odd and even modes for different silicon thicknesses $2d$ in the upper bandgap, as shown in Figs. 7(a) and 7(b), respectively. Both dispersion curves shift to the left as d decreases. For

a given frequency (ω), the propagation constant (k) of the even mode gradually approaches zero ($k_{\text{even}} \rightarrow 0$), but $k_{\text{even}} \neq 0$ as d decreases, whose dispersion is the same as that of the conventional InSb-Si-Metal waveguides [36]. In contrast to the even mode, the most significant difference from the odd mode is the presence of the INZ mode ($k_{\text{odd}} = 0$). As an example, the corresponding frequency for the INZ odd mode is $\omega = 1.0517\omega_p$ when $d = 0.04\lambda_p$, marked by the red dot in Fig. 7(b). Unlike the regular even and odd modes, this INZ odd mode exhibits a stable phase. To clearly verify this, we perform full-wave simulations of the INZ mode at $\omega = 1.0517\omega_p$, as seen in the right inset of Fig. 7(b). For comparison, the result for the regular odd mode when $d = 0.02\lambda_p$ is displayed in the left inset. It clearly demonstrates the zero-phase-shift transmission of the INZ odd mode, which is consistent with the theoretical results.

Next, utilizing the INZ odd USMP mode, we design a structure to achieve phase modulation with a phase shift of 2π , as shown in Fig. 7(c). This structure consists of two symmetric waveguides with different d , and the left part with $2d_1$ supports a non-INZ odd mode, while the right part with $2d_2$ supports an INZ odd mode. The point source (marked by the star) is positioned at a distance of L_x from the interface (dashed line). By adjusting L_x , we can precisely control the output phase ranging from $-\pi$ to π . To verify this, we perform simulations for different L_x values at $\omega = 1.0517\omega_p$. As an example, $d_1 = 0.02\lambda_p$ and $d_2 = 0.04\lambda_p$, corresponding to the green and red dots. Figure 7(d) shows the simulated H_z field amplitudes for

$L_x = 279.5$ um, 325.25 um, and 389 um, with the corresponding output phases being $-\pi$, 0 , and π . To more clearly demonstrate this, we plot the phase of the H_z field along the lower InSb-Si interface for these three L_x values, as shown in Fig. 7(e). As expected, the output phases are $-\pi$, 0 , and π due to the 'super-coupling' effect [56]. These results show that our waveguide can realize all-optical phase modulation with a phase shift ranging from $-\pi$ to π .

IV. CONCLUSION

In this work, we have proposed and investigated a slab waveguide consisting of a dielectric layer sandwiched between two semiconductors subjected to opposite external magnetic fields. The dispersion characteristics of SMPs are analytically derived in both local and non-local models. Our numerical results show that the waveguide supports two truly USMP modes in the upper bulk mode bandgap, owing to topological protection. However, in the lower bulk mode bandgap, SMPs lose their strict unidirectionality due to non-local effects. By leveraging the two USMP modes, we demonstrate a magnetically-controllable USMMI at THz frequencies. Notably, USMMI exhibits strong robustness against defects, with no backscattering, in contrast to conventional bidirectional waveguides, which are susceptible to backscattering. Furthermore, we realized a frequency- and magnetically-tunable arbitrary-ratio splitter based on robust USMMI, enabling precise control of the splitter's properties. Additionally, multimode conversion is achieved based on the splitter. We also identify a unique index-near-zero (INZ) odd USMP mode supported by our waveguide, distinct from conventional InSb-Si-Metal waveguides. Utilizing the INZ mode with zero phase shift transmission, we have designed a phase modulator that precisely controls the phase from $-\pi$ to π . These results in mode manipulation utilizing USMP - encompassing interference, power, and phase control - offer a novel approach for the flexible manipulation of THz topological waves.

ACKNOWLEDGMENTS

This work was supported by National Natural Science Foundation of China (12464057, 12104203, 12264027, 61927813); Natural Science Foundation of Jiangxi Province (20242BAB25039, 20224BAB211015, 20242BAB20030, 20242BAB20024); Jiangxi Double-Thousand Plan (jxsq2023101069); Research Program of NUDT (ZK22-17). K. L. Tsakmakidis acknowledges funding within the framework of the National Recovery and Resilience Plan Greece 2.0, funded by the European Union NextGenerationEU (Implementation body: HFRI), under Grant No. 16909. K. L. Tsakmakidis was also supported by the General Secretariat for Research and Technology and the Hellenic Foundation for Research

and Innovation under Grant No. 4509.

Appendix A: Derivation of dispersion formula in local model

In this appendix, we demonstrate Eq. (3) in the main text. In the local model, the magnetic field of SMP has non-zero components

$$\begin{aligned} H_{z_1} &= A e^{-\alpha_1 y} e^{i(kx - \omega t)}, & y \geq d \\ H_z &= (G_1 e^{\alpha_d y} + G_2 e^{-\alpha_d y}) e^{i(kx - \omega t)}, & -d < y < d \\ H_{z_2} &= C e^{\alpha_2 y} e^{i(kx - \omega t)}, & y \leq -d \end{aligned} \quad (\text{A1})$$

for the upper semiconductor layer, middle dielectric layer, and lower semiconductor layer, respectively. Using Maxwell's equations $\nabla \times \mathbf{H} = -i\omega\epsilon_0\epsilon_\infty \mathbf{E}$ and $\nabla \times \mathbf{E} = i\omega\mu_0 \mathbf{H}$, the non-zero components (E_x and E_y) of the electric field in each layer can be directly derived from H_z in Eq. (A1), thus E_x can be written as

$$\begin{aligned} E_{x_1} &= -\frac{(i\alpha_1\epsilon_{1_1} - ik\epsilon_{2_1})}{\omega\epsilon_0\epsilon_{v_1}\epsilon_{1_1}} A e^{-\alpha_1 y} e^{i(kx - \omega t)}, & y \geq d \\ E_x &= -\frac{\alpha_d}{i\omega\epsilon_0\epsilon_r} (G_1 e^{\alpha_d y} - G_2 e^{-\alpha_d y}) e^{i(kx - \omega t)}, & -d < y < d \\ E_{x_2} &= \frac{(i\alpha_2\epsilon_{1_2} - ik\epsilon_{2_2})}{\omega\epsilon_0\epsilon_{v_2}\epsilon_{1_2}} C e^{-\alpha_2 y} e^{i(kx - \omega t)}, & y \leq -d \end{aligned} \quad (\text{A2})$$

According to the boundary conditions of fields, H_z and E_x are continuous at boundaries $y = -d$ and $y = d$. Considering the continuity of H_z , which requires $H_{z_1}|_{y=d} = H_z|_{y=d} = H_{z_2}|_{y=-d} = H_z|_{y=-d}$, we obtain from Eq. (A1)

$$\begin{aligned} A e^{-\alpha_1 d} &= G_1 e^{\alpha_d d} + G_2 e^{-\alpha_d d} \\ C e^{-\alpha_2 d} &= G_1 e^{-\alpha_d d} + G_2 e^{\alpha_d d} \end{aligned} \quad (\text{A3})$$

Considering the continuity of E_x , which satisfies $E_{x_1}|_{y=d} = E_x|_{y=d} = E_{x_2}|_{y=-d} = E_x|_{y=-d}$, we obtain from Eq. (A2)

$$\begin{aligned} (k \frac{\epsilon_{2_1}}{\epsilon_{1_1}} - \alpha_1) A e^{-\alpha_1 d} &= \epsilon_{v_1} \frac{\alpha_d}{\epsilon_r} (G_1 e^{\alpha_d d} - G_2 e^{-\alpha_d d}) \\ (k \frac{\epsilon_{2_2}}{\epsilon_{1_2}} - \alpha_2) C e^{-\alpha_2 d} &= \epsilon_{v_2} \frac{\alpha_d}{\epsilon_r} (G_2 e^{\alpha_d d} - G_1 e^{-\alpha_d d}) \end{aligned} \quad (\text{A4})$$

By eliminating the four coefficients A , C , G_1 and G_2 in Eqs. (A3) and (A4), the dispersion relation of SMPs can be derived as

$$e^{4\alpha_d d} = \frac{[1 - \frac{\epsilon_r(\epsilon_{1_1}\alpha_1 - k\epsilon_{2_1})}{\epsilon_{1_1}\alpha_d\epsilon_{v_1}}][1 - \frac{\epsilon_r(\epsilon_{1_2}\alpha_2 - k\epsilon_{2_2})}{\epsilon_{1_2}\alpha_d\epsilon_{v_2}}]}{[1 + \frac{\epsilon_r(\epsilon_{1_1}\alpha_1 - k\epsilon_{2_1})}{\epsilon_{1_1}\alpha_d\epsilon_{v_1}}][1 + \frac{\epsilon_r(\epsilon_{1_2}\alpha_2 - k\epsilon_{2_2})}{\epsilon_{1_2}\alpha_d\epsilon_{v_2}}]} \quad (\text{A5})$$

which corresponds to Eq. (3) of the main text.

Appendix B: Derivation of formula in non-local model

In this appendix, we demonstrate Eq. (6) in the main text. When non-local effects are taken into account, the dispersion relation of SMP can be derived by solving the hydrodynamic and Maxwell's equations as follows [39]

$$\begin{aligned}\nabla \times \mathbf{H} &= -i\omega\varepsilon_0\varepsilon_\infty \mathbf{E} + \mathbf{J} \\ \nabla \times \mathbf{E} &= i\omega\mu_0 \mathbf{H} \\ \beta^2 \nabla(\nabla \cdot \mathbf{J}) + \omega(\omega + i\nu)\mathbf{J} + i\omega\mathbf{J} \times \omega_c \hat{z} &= i\omega\omega_p^2 \varepsilon_0 \varepsilon_\infty \mathbf{E}\end{aligned}\quad (\text{B1})$$

Since the SDS waveguide only supports the TM mode ($H_x = H_y = E_z = 0$), the above equations for the lossless case ($\nu = 0$) can be expressed as

$$\begin{aligned}\frac{\partial \tilde{E}_y}{\partial x} - \frac{\partial \tilde{E}_x}{\partial y} &= i\omega\mu_0 \tilde{H}_z \\ \frac{\partial \tilde{H}_z}{\partial y} &= -i\omega\varepsilon_0\varepsilon_\infty \tilde{E}_x + \tilde{J}_x \\ -\frac{\partial \tilde{H}_z}{\partial y} &= -i\omega\varepsilon_0\varepsilon_\infty \tilde{E}_y + \tilde{J}_y \\ \beta^2 \left[\frac{\partial^2 \tilde{J}_x}{\partial x^2} + \frac{\partial^2 \tilde{J}_y}{\partial x \partial y} \right] + \omega^2 \tilde{J}_x + i\omega\omega_c \tilde{J}_y &= i\omega\omega_p^2 \varepsilon_0 \varepsilon_\infty \tilde{E}_x \\ \beta^2 \left[\frac{\partial^2 \tilde{J}_x}{\partial x \partial y} + \frac{\partial^2 \tilde{J}_y}{\partial y^2} \right] + \omega^2 \tilde{J}_y - i\omega\omega_c \tilde{J}_x &= i\omega\omega_p^2 \varepsilon_0 \varepsilon_\infty \tilde{E}_y\end{aligned}\quad (\text{B2})$$

In the non-local model, the non-zero field components ($\tilde{E}_x, \tilde{E}_y, \tilde{H}_z$) and the normal component (\tilde{J}) are found to have the form [47]

$$\begin{aligned}\tilde{E}_{x1} &= (A_1 \exp^{ip_1 y} + A'_1 e^{-\gamma_1 y}) e^{i(kx - \omega t)} \\ \tilde{E}_{y1} &= -i(s_1 A_1 e^{ip_1 y} + s'_1 A'_1 e^{-\gamma_1 y}) e^{i(kx - \omega t)} \\ \tilde{H}_{z1} &= \frac{i}{\omega\mu_0} (L_1 A_1 e^{ip_1 y} + L'_1 A'_1 e^{-\gamma_1 y}) e^{i(kx - \omega t)} \quad y \geq d \\ \tilde{J}_{y1} &= -ik\tilde{H}_{z1} + i\omega\varepsilon_0\varepsilon_\infty \tilde{E}_{y1}\end{aligned}\quad (\text{B3})$$

for the upper semiconductor, and they can be written as

$$\begin{aligned}\tilde{E}_{x2} &= (A_2 e^{-ip_2 y} + A'_2 e^{\gamma_2 y}) e^{i(kx - \omega t)} \\ \tilde{E}_{y2} &= i(s_2 A_2 e^{-ip_2 y} + s'_2 A'_2 e^{\gamma_2 y}) e^{i(kx - \omega t)} \\ \tilde{H}_{z2} &= -\frac{i}{\omega\mu_0} (L_2 A_2 e^{-ip_2 y} + L'_2 A'_2 e^{\gamma_2 y}) e^{i(kx - \omega t)} \quad y \leq -d \\ \tilde{J}_{y2} &= -ik\tilde{H}_{z2} + i\omega\varepsilon_0\varepsilon_\infty \tilde{E}_{y2}\end{aligned}\quad (\text{B4})$$

For the lower semiconductor, the parameters are given in the main text. According to the continuous boundary conditions of electric fields, we have $\tilde{E}_{x1}|_{y=d} = \tilde{E}_{x2}|_{y=d}$ and $\tilde{E}_{x2}|_{y=-d} = \tilde{E}_{x1}|_{y=-d}$. Combining this with the first equations in Eq. (B3) and Eq. (B4) and the second equations in Eq. (A2), it is found that

$$\begin{aligned}A_1 e^{ip_1 d} + A'_1 e^{-\gamma_1 d} &= -\frac{\alpha_d}{i\omega\varepsilon_0\varepsilon_r} (G_1 e^{\alpha_d d} - G_2 e^{-\alpha_d d}) \\ A_2 e^{ip_2 d} + A'_2 e^{-\gamma_2 d} &= -\frac{\alpha_d}{i\omega\varepsilon_0\varepsilon_r} (G_1 e^{-\alpha_d d} - G_2 e^{\alpha_d d})\end{aligned}\quad (\text{B5})$$

According to the continuous boundary conditions of magnetic fields, $\tilde{H}_{z1}|_{y=d} = \tilde{H}_{z2}|_{y=d}$ and $\tilde{H}_{z2}|_{y=-d} = \tilde{H}_{z1}|_{y=-d}$. By combining the third equation in Eqs. (B3) and (B4) with the second equation in Eq. (A1), we obtain

$$\begin{aligned}\frac{i}{\omega\mu_0} (L_1 A_1 e^{ip_1 d} + L'_1 A'_1 e^{-\gamma_1 d}) &= G_1 e^{\alpha_d d} + G_2 e^{-\alpha_d d} \\ -\frac{i}{\omega\mu_0} (L_2 A_2 e^{ip_2 d} + L'_2 A'_2 e^{-\gamma_2 d}) &= G_1 e^{-\alpha_d d} + G_2 e^{\alpha_d d}\end{aligned}\quad (\text{B6})$$

Unlike in the local model, an additional boundary condition is required: $\mathbf{J} \cdot \hat{y} = 0$ [43] at InSb-Si interface, which can be written as $\tilde{J}_{y1}|_{y=d} = 0$ and $\tilde{J}_{y2}|_{y=-d} = 0$. Using the last equations from Eq. (B3) and Eq. (B4), we have

$$\begin{aligned}R_1 A_1 e^{ip_1 d} + R'_1 A'_1 e^{-\gamma_1 d} &= 0 \\ R_2 A_2 e^{ip_2 d} + R'_2 A'_2 e^{-\gamma_2 d} &= 0\end{aligned}\quad (\text{B7})$$

where $R_j = \frac{k}{\omega\mu_0} L_j + \omega\varepsilon_0\varepsilon_\infty s_j$ and $R'_j = \frac{k}{\omega\mu_0} L'_j + \omega\varepsilon_0\varepsilon_\infty s'_j$, with $L_j = -ks_j + ip_j$ and $L'_j = -ks'_j - \gamma_j$, $j = 1, 2$. By eliminating the six coefficients $A_1, A_2, A'_1, A'_2, G_1$ and G_2 in Eqs. (B5)- Eq. (B7), the dispersion relation of SMPs can be derived as

$$e^{4\alpha_d d} = \prod_{j=1}^2 N_j \quad (\text{B8})$$

with

$$N_j = \frac{\varepsilon_\infty \alpha_d / \varepsilon_r (\gamma_j s_j + ip_j s'_j) + k(\gamma_j + ip_j) + (k^2 - k_0^2 \varepsilon_\infty)(s'_j - s_j)}{\varepsilon_\infty \alpha_d / \varepsilon_r (\gamma_j s_j + ip_j s'_j) - k(\gamma_j + ip_j) - (k^2 - k_0^2 \varepsilon_\infty)(s'_j - s_j)}$$

which corresponds to Eq. (6) of the main text.

-
- [1] L. Lu, J. D. Joannopoulos, and M. Soljačić, Topological photonics, *Nat. Photonics* **8**, 821 (2014).
[2] Y. Hu, M. Tong, T. Jiang, J.-H. Jiang, H. Chen, and Y. Yang, Observation of two-dimensional time-

- reversal broken non-Abelian topological states, *Nat. Commun.* **15**, 10036 (2024).
[3] F. R. Prudêncio and M. G. Silveirinha, Ill-Defined Topological Phases in Local Dispersive Photonic Crystals,

- Phys. Rev. Lett. **129**, 133903 (2022).
- [4] C. A. Rosiek, G. Arregui, A. Vladimirova, M. Albrechtsen, B. Vosoughi Lahijani, R. E. Christiansen, and S. Stobbe, Observation of strong backscattering in valley-Hall photonic topological interface modes, *Nat. Photonics* **17**, 386 (2023).
 - [5] B. Bahari, A. Ndao, F. Vallini, A. El Amili, Y. Fainman, and B. Kanté, Nonreciprocal lasing in topological cavities of arbitrary geometries, *Science* **358**, 636 (2017).
 - [6] Z.-X. Gao, J.-Z. Liao, F.-L. Shi, K. Shen, F. Ma, M. Chen, X.-D. Chen, and J.-W. Dong, Observation of Unidirectional Bulk Modes and Robust Edge Modes in Triangular Photonic Crystals, *Laser & Photonics Reviews* **17**, 2201026 (2023).
 - [7] X. Yu, J. Chen, Z.-Y. Li, and W. Liang, Topological large-area one-way transmission in pseudospin-field-dependent waveguides using magneto-optical photonic crystals, *Photon. Res.* **11**, 1105 (2023).
 - [8] X. Ao, Z. Lin, and C. T. Chan, One-way edge mode in a magneto-optical honeycomb photonic crystal, *Phys. Rev. B* **80**, 033105 (2009).
 - [9] A. B. Khanikaev and A. Alù, Topological photonics: robustness and beyond, *Nat. Commun.* **15**, 931 (2024).
 - [10] Y. Hadad and B. Z. Steinberg, Magnetized Spiral Chains of Plasmonic Ellipsoids for One-Way Optical Waveguides, *Phys. Rev. Lett.* **105**, 233904 (2010).
 - [11] J. Chen and Z.-Y. Li, Prediction and Observation of Robust One-Way Bulk States in a Gyromagnetic Photonic Crystal, *Phys. Rev. Lett.* **128**, 257401 (2022).
 - [12] F. D. M. Haldane and S. Raghu, Possible Realization of Directional Optical Waveguides in Photonic Crystals with Broken Time-Reversal Symmetry, *Phys. Rev. Lett.* **100**, 013904 (2008).
 - [13] R. E. Prange and S. M. Girvin, *The Quantum Hall Effect* (Springer, New York, 1987).
 - [14] J. D. Joannopoulos, R. D. Meade, and J. N. Winn, *Photonic Crystals: Molding the Flow of Light*, 2nd ed. (Princeton University Press, Princeton, NJ, 2008).
 - [15] Z. Wang, Y. D. Chong, J. D. Joannopoulos, and M. Soljačić, Reflection-Free One-Way Edge Modes in a Gyromagnetic Photonic Crystal, *Phys. Rev. Lett.* **100**, 013905 (2008).
 - [16] L. Lu, H. Gao, and Z. Wang, Topological one-way fiber of second Chern number, *Nat. Commun.* **9**, 5384 (2018).
 - [17] Z. Wang, Y. D. Chong, J. D. Joannopoulos, and M. Soljačić, Observation of unidirectional backscattering-immune topological electromagnetic states, *Nature* **461**, 772 (2009).
 - [18] Y. Poo, R.-x. Wu, Z. Lin, Y. Yang, and C. T. Chan, Experimental Realization of Self-Guiding Unidirectional Electromagnetic Edge States, *Phys. Rev. Lett.* **106**, 093903 (2011).
 - [19] M. Wang, R.-Y. Zhang, L. Zhang, D. Wang, Q. Guo, Z.-Q. Zhang, and C. T. Chan, Topological One-Way Large-Area Waveguide States in Magnetic Photonic Crystals, *Phys. Rev. Lett.* **126**, 067401 (2021).
 - [20] P. Zhou, G.-G. Liu, Y. Yang, Y.-H. Hu, S. Ma, H. Xue, Q. Wang, L. Deng, and B. Zhang, Observation of Photonic Antichiral Edge States, *Phys. Rev. Lett.* **125**, 263603 (2020).
 - [21] F. Chen, H. Xue, Y. Pan, M. Wang, Y. Hu, L. Zhang, Q. Chen, S. Han, G.-g. Liu, Z. Gao, P. Zhou, W. Yin, H. Chen, B. Zhang, and Y. Yang, Multiple Brillouin Zone Winding of Topological Chiral Edge States for Slow Light Applications, *Phys. Rev. Lett.* **132**, 156602 (2024).
 - [22] G.-G. Liu, S. Mandal, X. Xi, Q. Wang, C. Devescovi, A. Morales-Pérez, Z. Wang, L. Yang, R. Banerjee, Y. Long, Y. Meng, P. Zhou, Z. Gao, Y. Chong, A. García-Etxarri, M. G. Vergniory, and B. Zhang, Photonic axion insulator, *Science* **387**, 162 (2025).
 - [23] Z. Yu, G. Veronis, Z. Wang, and S. Fan, One-Way Electromagnetic Waveguide Formed at the Interface between a Plasmonic Metal under a Static Magnetic Field and a Photonic Crystal, *Phys. Rev. Lett.* **100**, 023902 (2008).
 - [24] B. Hu, Q. J. Wang, and Y. Zhang, Broadly tunable one-way terahertz plasmonic waveguide based on nonreciprocal surface magneto plasmons, *Opt. Lett.* **37**, 1895 (2012).
 - [25] W. Gao, B. Yang, M. Lawrence, F. Fang, B. Béri, and S. Zhang, Photonic Weyl degeneracies in magnetized plasma, *Nat. Commun.* **7**, 12435 (2016).
 - [26] K. L. Tsakmakidis, K. Baskourellos, and T. Stefański, Topological, nonreciprocal, and multiresonant slow light beyond the time-bandwidth limit, *Appl. Phys. Lett.* **119**, 190501 (2021).
 - [27] D. E. Fernandes and M. G. Silveirinha, Topological Origin of Electromagnetic Energy Sinks, *Phys. Rev. Appl.* **12**, 014021 (2019).
 - [28] T. Ozawa, H. M. Price, A. Amo, N. Goldman, M. Hafezi, L. Lu, M. C. Rechtsman, D. Schuster, J. Simon, O. Zilberberg, and I. Carusotto, Topological photonics, *Rev. Mod. Phys.* **91**, 015006 (2019).
 - [29] S. Li, K. L. Tsakmakidis, T. Jiang, Q. Shen, H. Zhang, J. Yan, S. Sun, and L. Shen, Unidirectional guided-wave-driven metasurfaces for arbitrary wavefront control, *Nat. Commun.* **15**, 5992 (2024).
 - [30] X. Deng, L. Hong, X. Zheng, and L. Shen, One-way regular electromagnetic mode immune to backscattering, *Appl. Opt.* **54**, 4608 (2015).
 - [31] L. Hong, Y. You, Q. Shen, Y. Wang, X. Liu, H. Zhang, C. Wu, L. Shen, X. Deng, and S. Xiao, Magnetic field assisted beam-scanning leaky-wave antenna utilizing one-way waveguide, *Sci. Rep.* **9**, 16777 (2019).
 - [32] Y. Zhou, P. He, S. Xiao, F. Kang, L. Hong, Y. Shen, Y. Luo, and J. Xu, Realization of tunable index-near-zero modes in nonreciprocal magneto-optical heterostructures, *Opt. Express* **30**, 27259 (2022).
 - [33] K. L. Tsakmakidis, O. Hess, R. W. Boyd, and X. Zhang, Ultraslow waves on the nanoscale, *Science* **358**, eaan5196 (2017).
 - [34] J. Xu, Y. Luo, K. Yong, K. Baskourellos, and K. L. Tsakmakidis, Topological and high-performance nonreciprocal extraordinary optical transmission from a guided mode to free-space radiation, *Commun. Phys.* **6**, 1 (2023).
 - [35] L. Shen, J. Xu, Y. You, K. Yuan, and X. Deng, One-Way Electromagnetic Mode Guided by the Mechanism of Total Internal Reflection, *IEEE Photon. Technol. Lett.* **30**, 133 (2018).
 - [36] K. L. Tsakmakidis, L. Shen, S. A. Schulz, X. Zheng, J. Upham, X. Deng, H. Altug, A. F. Vakakis, and R. W. Boyd, Breaking Lorentz reciprocity to overcome the time-bandwidth limit in physics and engineering, *Science* **356**, 1260 (2017).
 - [37] L. Shen, Y. You, Z. Wang, and X. Deng, Backscattering-immune one-way surface magnetoplasmons at terahertz frequencies, *Opt. Express* **23**, 950 (2015).
 - [38] D. Jin, L. Lu, Z. Wang, C. Fang, J. D. Joannopoulos,

- M. Soljačić, L. Fu, and N. X. Fang, Topological magnetoplasmon, *Nat. Commun.* **7**, 13486 (2016).
- [39] S. A. H. Gangaraj and F. Monticone, Do truly unidirectional surface plasmon-polaritons exist?, *Optica* **6**, 1158 (2019).
- [40] J. J. Brion, R. F. Wallis, A. Hartstein, and E. Burstein, Theory of Surface Magnetoplasmons in Semiconductors, *Phys. Rev. Lett.* **28**, 1455 (1972).
- [41] K. L. Tsakmakidis, Y. You, T. Stefański, and L. Shen, Nonreciprocal cavities and the time-bandwidth limit: comment, *Optica* **7**, 1097 (2020).
- [42] S. Raza, S. I. Bozhevolnyi, M. Wubs, and N. Asger Mortensen, Nonlocal optical response in metallic nanostructures, *J. Phys.: Condens. Matter* **27**, 183204 (2015).
- [43] S. Buddhiraju, Y. Shi, A. Song, C. Wojcik, M. Minkov, I. A. D. Williamson, A. Dutt, and S. Fan, Absence of unidirectionally propagating surface plasmon-polaritons at nonreciprocal metal-dielectric interfaces, *Nat. Commun.* **11**, 674 (2020).
- [44] K. Baskourellos, O. Tsilipakos, T. Stefański, S. F. Galata, E. N. Economou, M. Kafesaki, and K. L. Tsakmakidis, Topological extraordinary optical transmission, *Phys. Rev. Res.* **4**, L032011 (2022).
- [45] F. Monticone, A truly one-way lane for surface plasmon polaritons, *Nat. Photonics* **14**, 461 (2020).
- [46] Y. Liang, S. Pakniyat, Y. Xiang, J. Chen, F. Shi, G. W. Hanson, and C. Cen, Tunable unidirectional surface plasmon polaritons at the interface between gyrotropic and isotropic conductors, *Optica* **8**, 952 (2021).
- [47] J. Yan, Q. Shen, H. Zhang, S. Li, H. Tang, and L. Shen, Broadband unidirectional surface plasmon polaritons with low loss, *Opt. Express* **31**, 35313 (2023).
- [48] L. Liu, Y. Wang, F. Zheng, and T. Sang, Multimode interference in topological photonic heterostructure, *Opt. Lett.* **47**, 2634 (2022).
- [49] X. Ma, Y. Li, Q. Xu, and J. Han, Terahertz plasmonic functional devices enabled by multimode interference, *Opt. Laser Technol.* **171**, 110391 (2024).
- [50] L. Liu and Y. Wang, Unidirectional mode interference in magneto-optical photonic heterostructure, *Opt. Laser Technol.* **161**, 109224 (2023).
- [51] S. A. Skirlo, L. Lu, and M. Soljačić, Multimode One-Way Waveguides of Large Chern Numbers, *Phys. Rev. Lett.* **113**, 113904 (2014).
- [52] W. Tang, M. Wang, S. Ma, C. T. Chan, and S. Zhang, Magnetically controllable multimode interference in topological photonic crystals, *Light Sci. Appl.* **13**, 112 (2024).
- [53] P. Halevi, Hydrodynamic model for the degenerate free-electron gas: Generalization to arbitrary frequencies, *Phys. Rev. B* **51**, 7497 (1995).
- [54] G. R. Fonseca, F. R. Prudêncio, M. G. Silveirinha, and P. A. Huidobro, First-principles study of topological invariants of Weyl points in continuous media, *Phys. Rev. Research* **6**, 013017 (2024).
- [55] L. Soldano and E. Pennings, Optical multi-mode interference devices based on self-imaging: Principles and applications, *J. Lightwave Technol.* **13**, 615 (1995).
- [56] N. Engheta, Pursuing Near-Zero Response, *Science* **340**, 286 (2013).